Eur. Phys. J. C (2025) 85:905
https://doi.org/10.1140/epjc/s10052-025-14654-4

THE EUROPEAN PHYSICAL JOURNAL C

Regular Article - Theoretical Physics

Shadows of three black holes in static equilibrium configuration

Dan Li[1], **Yuxiang Zuo**[1], **Shiyang Hu**[1,a], **Chen Deng**[2], **Yu Wang**[3], **Wenfu Cao**[4]

[1] School of Mathematics and Physics, University of South China, Hengyang 421001, People's Republic of China
[2] School of Astronomy and Space Science, Nanjing University, Nanjing 210023, People's Republic of China
[3] School of Physical Science and Technology, Guangxi University, Nanning 530004, People's Republic of China
[4] School of Physics and Technology, University of Jinan, Jinan 250022, People's Republic of China

Received: 9 April 2025 / Accepted: 17 August 2025

Abstract In this paper, we employ a ray-tracing algorithm to simulate the shadows of three equal-mass black holes in static equilibrium across a wide parameter space. We find that the shadows consist of a larger primary shadow and several distorted, eyebrow-like secondary shadows. The boundaries of these profiles exhibit self-similar fractal structures, which can be attributed to the photon chaotic scattering. In certain parameter spaces, we also observe the ring-like shadows, with the ring diameter associated with the spacing of black holes. Furthermore, when the black holes approach each other sufficiently, their shadows can merge into a standard disk, suggesting a shadow degeneracy between closely arranged triple black holes and a single massive, spherically symmetric black hole. The shadow features of the triple black holes revealed in this study have potential implications for analyzing the shadow formation mechanisms, as well as the gravitational lensing during the merger and inspiral of black holes.

Contents

1 Introduction

The images of the supermassive black holes at the center of Virgo (M87*) and the Milky Way (Sgr A*), released by the Event Horizon Telescope (EHT) Collaboration [1,2], represent a monumental milestone in astronomical exploration. These historic observations not only provide definitive confirmation of black holes' existence but also open a new avenue for studying black hole physics, gravitational theories, and high-energy astrophysics. Consequently, a surge of research has emerged on black hole shadow [3–22], gravitational lensing [23–27], holographic images of the Einstein ring [28–30], and accretion disk radiation [31–35]. However, current observational limitations constrain the EHT's targets to only M87* and Sgr A*, and the astrophysical information extractable from these images remains restricted.

The next-generation Event Horizon Telescope (ngEHT) project aims to significantly extend interferometric baselines by incorporating space-borne antennas, thereby achieving unprecedented imaging resolution [36–38]. This technological leap will not only enable more precise measurements of shadow geometry in M87* and Sgr A*, but also potentially expand observational capabilities to other black holes, compact objects, and even multiple black hole systems. Notably, observational evidence has already hinted at the existence of supermassive binary black holes and black hole clusters [39–41]. Investigating the imaging signatures of such systems could provide the scientific community with direct insights into the gravitational interactions, structural configurations, and evolution of multiple black hole systems.

In fact, numerous studies have investigated the shadow characteristics of binary black holes. Nitta et al. employed the Kastor–Traschen solution to model the contracting spacetime of a binary black hole system with a cosmological constant, numerically simulating the shadow evolution of colliding black holes driven by spacetime contraction [42]. The results demonstrated that as the binary black holes converge, their individual shadows undergo deformation and develop distinctive eyebrow-like secondary shadow. Build-

[a] e-mail: husy_arcturus@163.com (corresponding author)

Published online: 26 August 2025

ing on this work, Yumoto et al. conducted further investigations by deriving analytical expressions for photon motion in binary black hole spacetimes, thereby elucidating the formation mechanism of the eyebrow-like shadow. Through extensive numerical simulations across a broader parameter space, they additionally identified ring-shaped shadow structures [43]. The authors in [44] numerically simulated photon trajectories in binary black hole spacetime. By employing a fisheye projection technique, they visually reconstructed the black hole shadows and revealed self-similar fractal structures at the shadow boundaries. To further investigate how black hole spins influence binary black holes' shadow, Cunha et al. employed a ray-tracing algorithm to simulate shadows based on the double-Kerr solution. Their work demonstrated that spin alignment between the two black holes significantly modifies the resulting image features [45]. Meanwhile, the study in [46] focused specifically on photon ring formation in binary black hole system and its dependence on system parameters. Additional studies on binary black hole shadows can be found in [47,48]. Overall, the shadow characteristics of such system have been nearly exhaustively explored. This comprehensive understanding naturally leads us to pose the next fundamental question: What distinctive shadow features would manifest in a triple black hole system? Addressing this unexplored problem constitutes the primary motivation of the present study.

The triple black hole system resembles the classic and enigmatic three-body problem – without any constraints, the geodesic equations for particles in its spacetime become non-integrable due to violations of Liouville's integrability theorem. This poses significant challenges for studying such system. Moreover, constructing an exact analytical metric describing triple black holes is virtually impossible. Fortunately, when additional constraints are imposed on the triple black hole system, the target spacetime can be described by the Majumdar–Papapetrou solution [49,50]. In this scenario, the gravitational attraction between black holes is theoretically balanced by electrostatic repulsion, thereby allowing the three black holes to maintain a static equilibrium configuration. Hartle and Hawking demonstrated that when the black holes in the Majumdar–Papapetrou solution are extremal Reissner–Nordström (RN) black holes (i.e., $Q = M$, where Q and M represent the charge and mass of the black hole, respectively), the solution satisfies the source free Einstein–Maxwell field equations [51]. Moreover, as the Majumdar–Papapetrou metric is an exact analytical solution, it provides a tractable framework for investigating the shadows of triple black holes.

The remainder of this paper is organized as follows. Section 2 provides a concise review of the Majumdar–Papapetrou metric and derives the equations of motion for photons in this spacetime. Section 3 introduces the essential ray-tracing algorithm for simulating black hole shadows. In Sect. 4, we present the shadows of triple black holes across different parameter spaces, with detailed analysis of their distinctive features. The final section summarizes our findings. Throughout this work, we adopt geometric units with $G = c = M_s = 1$, where M_s denotes the total mass of three black holes.

2 Spacetime and geodesics

Theoretically, maintaining stable configurations of three static black holes in vacuum is extraordinarily challenging. However, such equilibrium becomes possible when all three black holes carry like-sign charges. In this scenario, the gravitational attraction between black holes is precisely counterbalanced by the electrostatic repulsion. The Majumdar–Papapetrou solution originates from this principle, describing spacetimes containing n static equilibrium black holes. In isotropic coordinates, the Majumdar–Papapetrou metric reads as [46,49,50,52]

$$\mathrm{d}s^2 = -\frac{\mathrm{d}t^2}{\mathcal{U}^2} + \mathcal{U}^2\left(\mathrm{d}x^2 + \mathrm{d}y^2 + \mathrm{d}z^2\right). \tag{1}$$

Here, $\mathcal{U}$ denotes the spacetime gravitational potential, given by

$$\mathcal{U} = 1 + \sum_{i=1}^{n} \frac{m_i}{r_i}, \tag{2}$$

where m_i represents the mass of the ith black hole, and r_i takes the form

$$r_i = \sqrt{(x - x_i)^2 + (y - y_i)^2 + (z - z_i)^2}. \tag{3}$$

Here, (x_i, y_i, z_i) denote the spatial coordinates of the black holes. Remarkably, these black holes maintain static equilibrium regardless of their spatial configuration. For our subsequent analysis, we set $n = 3$ and fix equal masses for all three black holes, i.e., $m_1 = m_2 = m_3 = M_s/3$. Consequently, we have the metric potential for three static black hole spacetime in geometric units,

$$\mathcal{V} = 1 + \sum_{i=1}^{3} \frac{1}{3r_i}. \tag{4}$$

Hence, we have

$$\mathrm{d}s^2 = -\frac{\mathrm{d}t^2}{\mathcal{V}^2} + \mathcal{V}^2\left(\mathrm{d}x^2 + \mathrm{d}y^2 + \mathrm{d}z^2\right). \tag{5}$$

In spacetime (5), the geodesic equations for photons are governed by canonical equations in the Hamiltonian frame. To this end, we first define the Lagrangian as

$$\mathcal{L} = \frac{1}{2}\left[-\frac{\dot{t}^2}{\mathcal{V}^2} + \mathcal{V}^2\left(\dot{x}^2 + \dot{y}^2 + \dot{z}^2\right)\right], \tag{6}$$

where the overdot denotes the derivatives of generalized coordinates with respect to an affine parameter λ, i.e., $\dot{t} = \mathrm{d}t/\mathrm{d}\lambda$. Then, through the Euler–Lagrange equations, we introduce the conjugate momenta

$$p_t = -\frac{1}{\mathcal{V}^2}\dot{t}, \tag{7}$$

and

$$p_\alpha = \mathcal{V}^2\dot{\alpha}, \tag{8}$$

where α runs from x to z. Applying the Legendre transformation $\mathcal{H} = \vec{p}\cdot\vec{v} - \mathcal{L}$ yields the Hamiltonian for photon motion in spacetime (5),

$$\mathcal{H} = \frac{1}{2}\left[-\mathcal{V}^2 p_t^2 + \frac{1}{\mathcal{V}^2}\left(p_x^2 + p_y^2 + p_z^2\right)\right]. \tag{9}$$

For photons, the Hamiltonian constraint is $\mathcal{H} = 0$, while for massive particles it becomes $\mathcal{H} = -1/2$. We note that the Hamiltonian (9) does not explicitly depend on the coordinate t. In fact, due to the time-translational invariance, p_t is a motion constant during the propagation of light rays, with its relation to the photon's specific energy E given by $p_t = -E$. From the Hamiltonian constraint, the photon's p_t can be determined given its three-momentum components,

$$p_t^2 = \frac{p_x^2 + p_y^2 + p_z^2}{\mathcal{V}^4}, \tag{10}$$

which is important in the determination of initial conditions during ray-tracing method described in the following section.

According to canonical equations, the propagation of light rays is governed by

$$\dot{t} = \frac{\partial\mathcal{H}}{\partial p_t},\ \dot{x} = \frac{\partial\mathcal{H}}{\partial p_x},\ \dot{y} = \frac{\partial\mathcal{H}}{\partial p_y},\ \dot{z} = \frac{\partial\mathcal{H}}{\partial p_z}, \tag{11}$$

$$\dot{p}_t = -\frac{\partial\mathcal{H}}{\partial t},\ \dot{p}_x = -\frac{\partial\mathcal{H}}{\partial x},\ \dot{p}_y = -\frac{\partial\mathcal{H}}{\partial y},\ \dot{p}_z = -\frac{\partial\mathcal{H}}{\partial z}. \tag{12}$$

Given the initial coordinates and momentum of a light ray $(t, x, y, z, p_t, p_x, p_y, p_z)$, we employ a fifth- and sixth-order Runge–Kutta–Fehlberg integrator with adaptive step sizes to integrate Eqs. (11) and (12), the photon path can be obtained.

3 Ray-tracing method

The study of black hole shadows necessitates the application of ray-tracing algorithms. While numerous sophisticated ray-tracing methods exist in the scientific literature [53–58] this investigation adopts the framework of ODYSSEY [59]. We employ a collinear three static black hole system to elucidate the ray-tracing procedure. As illustrated in Fig. 1, the spacetime containing three static black holes is parameterized using a local coordinate system xyz, with the three black holes designated as m_1, m_2, and m_3, respectively. Here, m_2 is positioned at the coordinate origin o, while the other two black holes are symmetrically distributed along the y-axis relative to m_2. The blue sphere in the figure represents the observer, whose local coordinate system is described by $x'y'z'$. Here, $\overline{oo'}$ coincides with $\overline{o'z'}$. We further define the observation angle Θ as the angle between $\overline{oo'}$ and the z-axis, and the observation azimuth Φ as the angle between the projection of the observer onto the $\overline{xoy}$ plane and the x-axis. The observed image is described by the $\overline{x'o'y'}$ plane. Notably, for the black hole configuration depicted in Fig. 1 – where three black holes are aligned along the y-axis – the resulting image depends on both the azimuthal angle Φ and the inclination Θ.

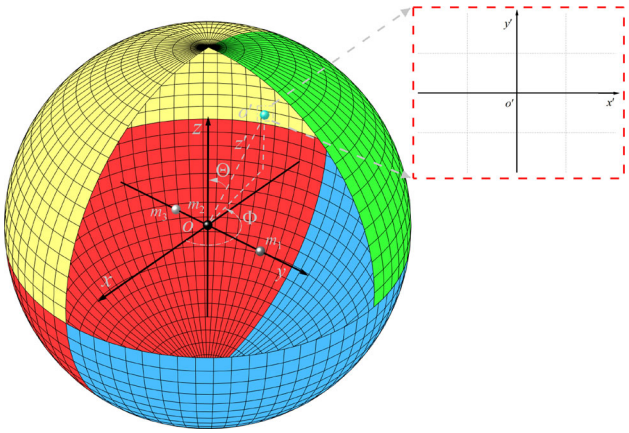

Fig. 1 Ray-tracing map and light source configuration in the triple static black holes' spacetime. The spatial configuration of the three black holes, m_1, m_2, and m_3, is described by the coordinate system xyz. The observer is represented by a blue sphere, with his local frame and field of view defined by the coordinate system $x'y'z'$ and $\overline{x'o'y'}$ plane (see zoomed-in view), respectively. Φ and Θ are azimuthal angle and inclination angle of the observer, respectively. We employ a spherical light source with a radius of 1500 M_s encompassing both the three black holes and the observer. Light rays emitted from the observation plane are captured by either m_1, m_2, or m_3, with their corresponding pixel coordinates filled in dark gray, black, or light gray, respectively. For rays that escape capture and subsequently strike the spherical light source, their pixel coordinates are color-coded according to intersection location: yellow ($z > 0$, $y < 0$), green ($z > 0$, $y > 0$), red ($z < 0$, $y < 0$), and blue ($z < 0$, $y > 0$)

To visualize the black hole shadows more intuitively, we employ a celestial light source with radius $r_{\mathrm{source}} = 1500\,M_s$ enveloping both the observer and the three black holes, as represented by the colored sphere in Fig. 1. Notably, the sphere consists of four distinct colors, while the three black holes are depicted in dark gray, black, and light gray, respectively. Consequently, when light rays emitted from the observation plane $\overline{x'o'y'}$ are captured by a black hole, their corresponding pixels are filled with either dark gray, black, or light gray.

For light rays that graze the black holes and subsequently hit the celestial sphere, their observation coordinates are marked with green, yellow, red, or blue, according to the hitting location.

Subsequently, we trace light rays emitted from each pixel on the observation plane within the black holes' local coordinate system. This requires determining the initial conditions of the light rays in the xyz frame. Through coordinate transformation, we have [59,60]

$$x = \mathscr{T}\cos\Phi - x'\sin\Phi, \tag{13}$$

$$y = \mathscr{T}\sin\Phi + x'\cos\Phi, \tag{14}$$

and

$$z = \left(r_{\rm obs} - z'\right)\cos\Theta + y'\sin\Theta, \tag{15}$$

in which $\mathscr{T}$ takes the form

$$\mathscr{T} = \left(r_{\rm obs} - z'\right)\sin\Theta - y'\cos\Theta. \tag{16}$$

Here, $r_{\rm obs}$ denotes the observation distance, and we fix it at 1000 M_s.

Since spacetime (5) is asymptotically flat, we can reasonably assume that light rays hit the observation plane orthogonally. In other word, the initial velocity of light rays satisfies $(\dot{x'}, \dot{y'}, \dot{z'}) = (0, 0, 1)$. Substituting this condition into the differential forms of (13)–(15) yields:

$$\dot{x} = -\sin\Theta\cos\Phi, \tag{17}$$

$$\dot{y} = -\sin\Theta\sin\Phi, \tag{18}$$

$$\dot{z} = -\cos\Theta. \tag{19}$$

From these, we derive the photon's three-momentum using definition (8), and subsequently determine p_t via (10). Thus, we obtain the initial conditions for light rays corresponding to each pixel on the observation plane. According to the canonical equations (11) and (12), the fate of each light ray can be precisely determined. Those rays that plunge into the black holes contribute to the black hole shadow.

4 Results

We focus on the shadows of triple black holes in two configurations: (i) A collinear configuration where all three black holes lie on a straight line. Here, black hole m_2 is positioned at the coordinate origin, while the other two black holes are symmetrically distributed along the y-axis at distances l from m_2. Their coordinates are $(0, l, 0)$, $(0, 0, 0)$, and $(0, -l, 0)$, respectively. (ii) An equilateral triangle configuration with side length l, where m_2 is located at $(\sqrt{3}l/2, 0, 0)$ and other two black holes are placed on the y-axis at $(0, l/2, 0)$ and $(0, -l/2, 0)$. For both configurations, the free parameters of the system are Θ, Φ, and l.

4.1 Collinear configuration

We set the observation plane with $x' \in [-8, 8]$ M_s and $y' \in [-6, 6]$ M_s at a resolution of 2400×1800 pixels. Figure 2 demonstrates the variation of triple black holes' shadow with l, where the dark gray, black, and light gray shadows are cast by m_1, m_2, and m_3, respectively. As clearly observed when the black holes are widely separated ($l = 4$), each shadow consists of multiple disjoint components, with the largest structure classified as the "primary shadow" and the eyebrow-like features termed "secondary shadows". For m_2, its primary shadow exhibits elongation toward both ends of the y'-axis, forming an elliptical shape, while its secondary shadows appear symmetrically outside the primary shadows of the other two black holes – this feature originate from photons grazing m_1 or m_3 before be captured by m_2. The m_1 and m_3 shadows form mirror images with respect to the y'-axis. Their primary shadows exhibit a tendency to converge toward the y'-axis, while the secondary shadows near the primary shadows of the other two black holes. The deformation of the primary shadows of m_1 and m_3 arises because the strong gravitational field on the left (right) side of m_1 (m_3) disrupts its inherent spacetime symmetry.

As l decreases, the shadows of the three black holes progressively approach each other while undergoing significant morphological changes. Notably for m_2, its primary shadow elongates from an elliptical shape into a columnar form, ultimately expanding into a perfect circle at $l = 0.1$ that envelops the other two black holes' shadows. In contrast, the primary shadows of m_1 and m_3 undergo relatively minor modifications – they morph into arch by $l = 0.7$ and subsequently remain nearly unchanged. However, their secondary shadows exhibit progressive elongation and distortion as l decreases. Interestingly, we find that when the three black holes are sufficiently close, their combined shadow becomes virtually indistinguishable from that of a single spherically symmetric black hole, as exemplified in panel (i). This demonstrates that the photon capture capability of three tightly packed black holes can be effectively mimicked by a single black hole. This degeneracy suggests a novel perspective on black hole internal structure: the event horizon of a single black hole might originate from multiple tightly packed extremal RN black holes in its interior. Moreover, in each panel, we detect image features near the shadow boundary that originate from distinct black holes. Although resolution limitations render these features only as discrete points or line segments, their alternating pattern remains identifiable. This phenomenon arises from chaotic scattering of photon due to the non-integrable nature of spacetime (5), generating self-similar fractal structures along the shadow boundary.

By varying the observer's azimuthal angle Φ to 45° and 90°, we further investigate the influence of l on the shadows of triple black holes, with the corresponding results dis-

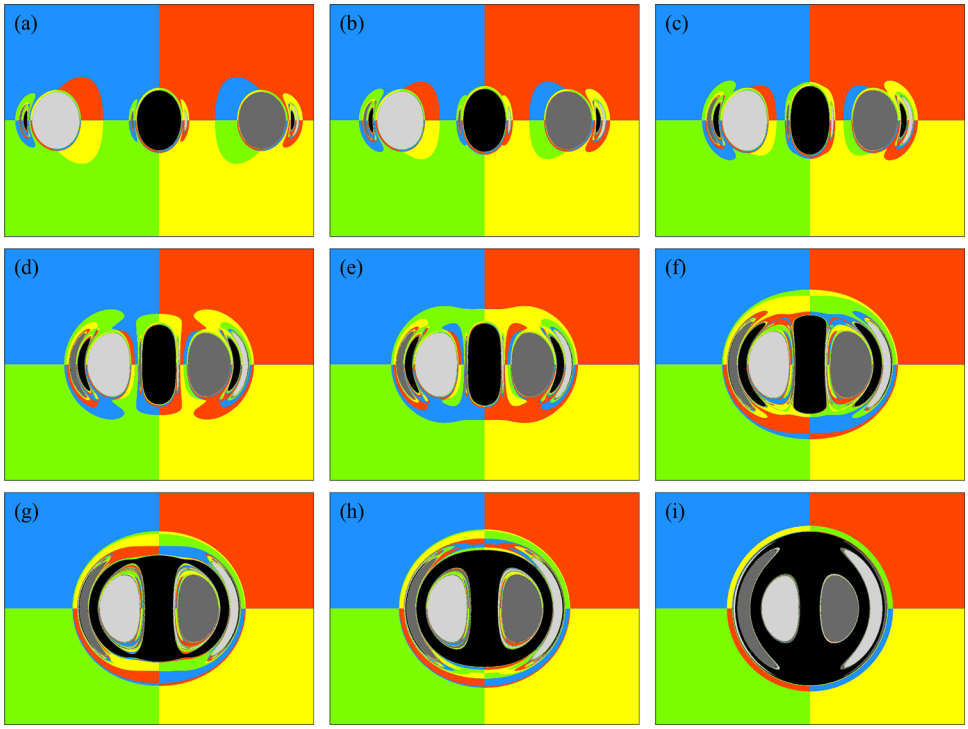

Fig. 2 Shadows of triple static black holes with varying parameter l. From panel **a** to panel **i**, l are 4, 3, 2, 1.2, 1.1, 0.7, 0.6, 0.5, and 0.1, respectively. Here, we have the observation angle $\Theta = 90°$ and azimuthal angle $\Phi = 0°$. In most panels, beyond the three prominent primary shadows, we clearly identify eyebrow-like secondary shadows generated by gravitational lensing. As the black holes approach each other, these secondary shadows exhibit increasing distortion and elongation. When the three black holes become sufficiently close ($l \leqslant 0.1$), their primary shadows merge into a single larger shadow. This behavior suggests a fundamental degeneracy between three tightly packed black holes and a single massive black hole in terms of their photon-capture capabilities

played in Figs. 3 and 4. At an observation azimuth of 45°, the position, size, and shape of m_1's primary shadow remain largely unaffected by the parameter l, while its two secondary shadows located leftward of the m_2 and m_3 exhibit progressive elongation as l decreases. Notably, at $l = 1$ (panel (d)), m_1 develops a third secondary shadow on the image's right side in addition to the two prominent left-side secondaries. This newly emerged shadow feature ultimately merges with the left-side secondaries to form a shadow ring as l further decreases, as demonstrated in panel (g). Similar evolutionary patterns occur for m_2 and m_3 – their primary and secondary shadows gradually coalesce into rings with diminishing l. Particularly for m_3, Fig. 3 clearly documents this ring formation process.

When the azimuthal angle reaches $\Phi = 90°$, the three black holes become colinearly aligned with the line of sight. In this configuration, m_1 produces a perfectly disk shadow, while m_2 and m_3 generate thick ring-like shadows through an Einstein-ring formation mechanism, with their ring radii showing a positive correlation with l. Since m_3 lies behind m_2, its ring shadow undergoes magnification by both m_1 and m_2, making it the largest among the three black holes. Additionally, we clearly identify thin ring-like shadows from all three black holes, which correspond to higher-order secondary shadows created by gravitational lensing. Notably, when l becomes sufficiently small, we observe the convergence of all three shadows into a single faint region.

Through Figs. 2, 3 and 4, we observe distinctive features in the shadows of triple black holes: ring-shaped shadow and eyebrow-like shadow. Although similar features have been identified in black hole binaries [42–45,47,48], scalar hairy black holes [61–63], and the single black hole with quadrupole or octupole distortions [64,65], their quantitative occurrence is lower than revealed in our study. Specifically, the number of these fine structures depends on both the count and spatial distribution of compact objects. This implies that multiple concentric ring-shaped shadows or clustered eyebrow-like shadows may serve as unique observational probes for triple black hole system. Furthermore, Figs. 2, 3 and 4 not only display shadows at varying spatial separations but also effectively trace the evolutionary sequence of shadows during the triple black holes merger process.

It is worth emphasizing that when spacetime perturbations induced by black hole motion are neglected, model (5) can qualitatively characterize snapshots of the dynamic triple black holes at arbitrary instants. This approach conveniently enables preliminary investigation of shadow evolution during the rotation or inspiral of such system. Accordingly, we (i) simulated the rotation of the triple black holes by continuously varying the observer's azimuthal angle while maintaining a fixed separation ($l = 2$) in the collinear configuration, with the resulting shadow evolution presented in Fig. 5; and (ii) simultaneously varied both the black hole separation and azimuthal angle to model shadow evolution during the inspi-

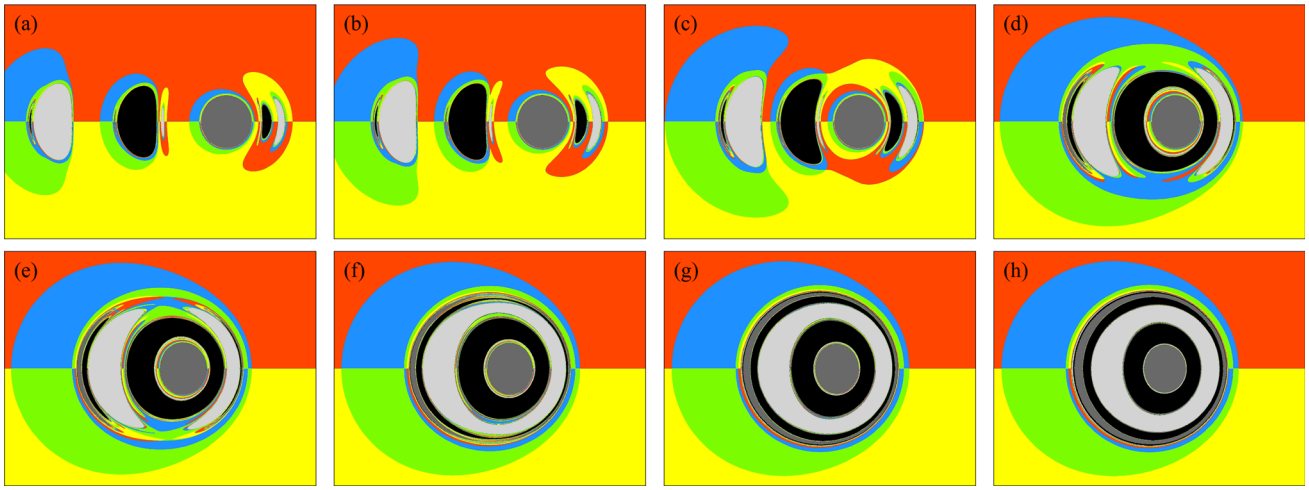

Fig. 3 Shadows of triple static black holes with different l. From panel **a** to panel **h**, the distance l are 4, 3, 2, 1, 0.75, 0.5, 0.25, and 0.1, respectively. Here, we have the observation angle $\Theta = 90°$ and azimuthal angle $\Phi = 45°$. The primary shadow of m_1 remains nearly invariant throughout the evolution, maintaining its quasi-circular morphology. In contrast, the primary shadows of m_2 and m_3 undergo a progressive transformation from arched to crescent-shaped profiles as l decreases, ultimately merging with their respective secondary shadows to form asymmetric rings. Notably, similar to Fig. 2, when l becomes sufficiently small ($l \leqslant 0.1$), all three shadows coalesce into a unified structure

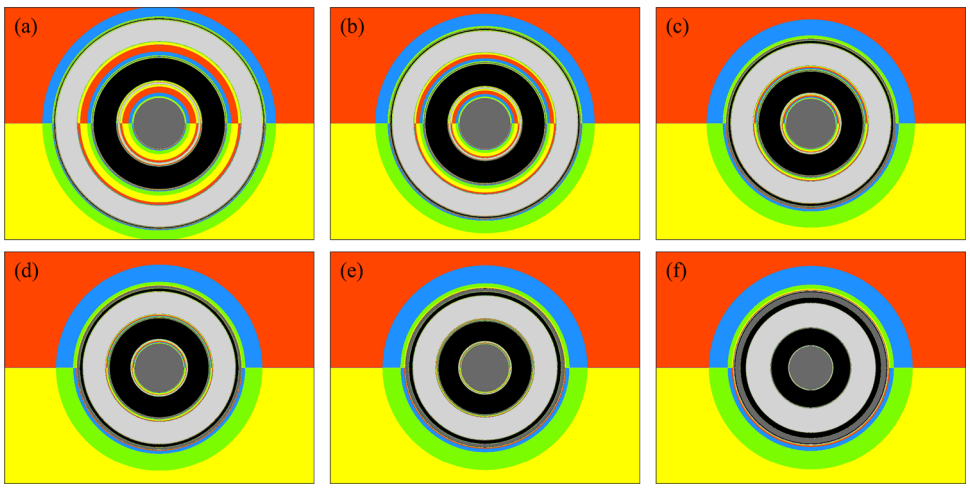

Fig. 4 Evolution of shadows of triple static black holes with parameter l. From panel **a** to panel **f**, the distance l are 3, 2, 1, 0.75, 0.5, and 0.1, respectively. Here, we have the observation angle $\Theta = 90°$ and azimuthal angle $\Phi = 90°$. We observe sequentially from the image center outward: the circular shadow of m_1, followed by the ring-like shadow of m_2, and finally the ring-like shadow of m_3. As l decreases, the ring shadows of both m_2 and m_3 exhibit significant contraction. At the critical separation $l = 0.1$, all three shadows coalesce into a perfect disk profile

ral phase, as shown in Fig. 6. In the former case, we find that when Φ changes from 0° to 30°, the primary shadow of the right black hole (m_1) becomes more circular, while the primary shadows of m_2 and m_3 exhibit crescent shapes eroded by m_1. This occurs because the right side of the observation screen represents the approaching side while the left corresponds to the receding side, placing m_2 and m_3 behind m_1 in panel (b). Simultaneously, we observe elongated multiple secondary shadows from all three black holes, with the most pronounced changes occurring in m_3's counterparts. As the azimuthal angle further increases, the primary and secondary shadows of m_2 become vertically connected and merge into a ring-like structure enveloping m_1's primary shadow due to lensing effects, while m_3's shadow continues to exhibit progressive elongation. When the three black holes rotate into alignment with the line of sight, ring-shaped shadows emerge – a phenomenon we have detailed in Fig. 4. As the orbital motion continues, we obtain an image that is symmetric with panel (c) about the y'-axis, resulting from m_1 having moved to the observer's left while m_3 has shifted to

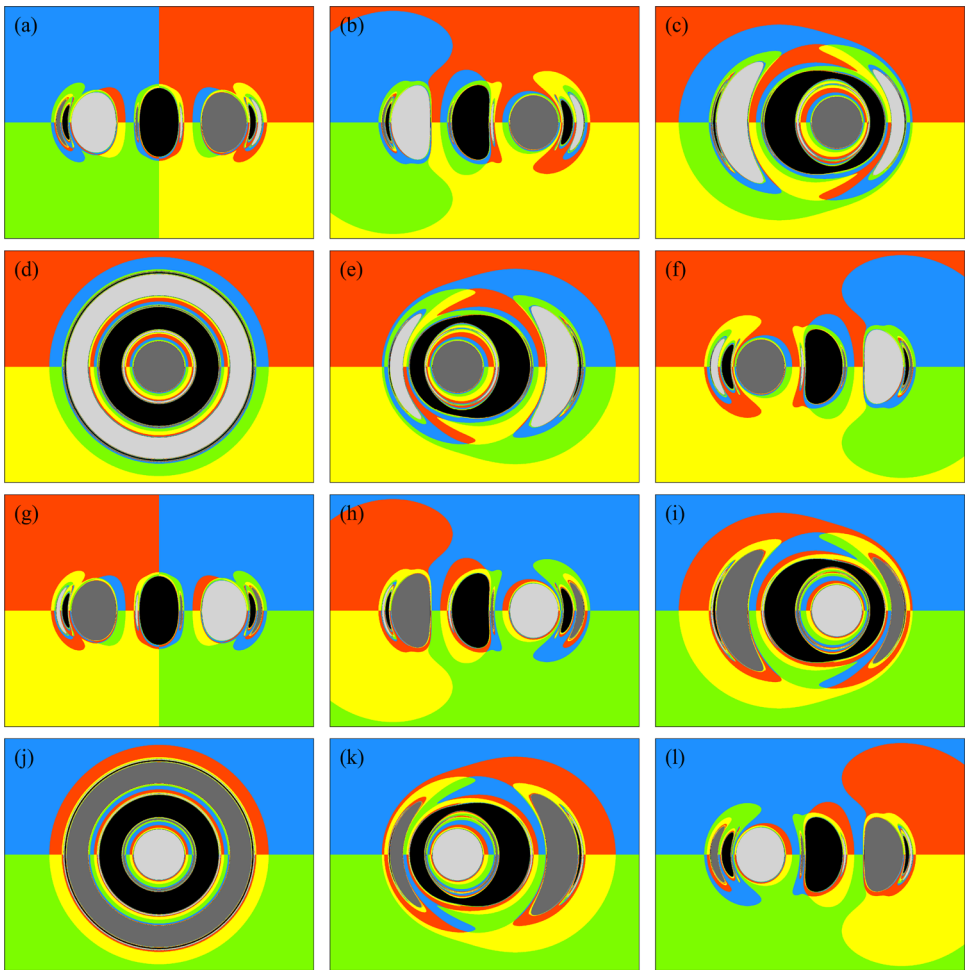

Fig. 5 Shadow evolution of triple static black holes under varying azimuthal angles Φ at fixed separation $l = 2$. Panels **a–l** display configurations from $\Phi = 0°$ to $\Phi = 330°$ in 30° increments, with a constant observation inclination of $\Theta = 90°$

the right. At $\Phi = 180°$, the three black holes complete a half-orbit, exchanging the positions of m_1 and m_3 relative to panel (a). For $\Phi > 180°$, the shadow configurations become mirror images about the y'-axis of their counterparts in panels (a)–(f), due to the system's intrinsic symmetry.

In Fig. 6, we find that during the early inspiral phase, such as panels (a)–(m), the image morphology depends more strongly on Φ than on separation l, as evidenced by shadow deformations nearly identical to those in Fig. 5. During this process, m_1's primary shadow remains nearly circular as it migrates from the right to the left side of the image, while its faint secondary shadows are only detectable upon magnification. Meanwhile, m_2's primary shadow transitions through a crescent phase, temporarily merges with its secondary shadows to form a coherent ring structure, and eventually fragments back into an elongated shape. Concurrently, m_3's primary shadow exhibits similar ring-like snapshots, completing its left-to-right positional shift during the ring fragmentation phase. During the late inspiral phase, the influence of the separation l on the image becomes pronounced. As l decreases, m_2's primary and secondary shadows first converge and envelop m_1's primary shadow. Subsequently, m_3's shadow replicates m_1's structural behavior along m_1's periphery. Ultimately, as shown in panel (r), the shadows of all three black holes become nearly indistinguishable, separated only by thin rings that gradually vanish with further decreasing l. In summary, Figs. 5 and 6 present the evolving shadow features of the triple black holes during their orbital, inspiral, and merger phases. These results characterize the deformation and motion of both primary and secondary shadows for each black hole, providing important insights for future observations of multi-black-hole systems.

Next, we investigate how the observation inclination Θ affects the images. Figure 7 illustrates the dependence of the triple black hole shadow on the inclination angle Θ, while maintaining fixed black hole separation l and systematically varying the observer's azimuthal angle Φ. The analysis reveals that the effects induced by Θ can be categorized into two distinct types. First type (panels (a)–(c) and (m)–(o)): Varying the inclination angle Θ does not alter the shadow contours of any of the three black holes – neither the primary nor secondary shadows exhibit morphological changes. Nevertheless, we can still identify changes in the background source distribution – that is, when accounting for source emission, luminosity variations with viewing angle are indeed expected. Second type (panels (d)–(l)): Increasing

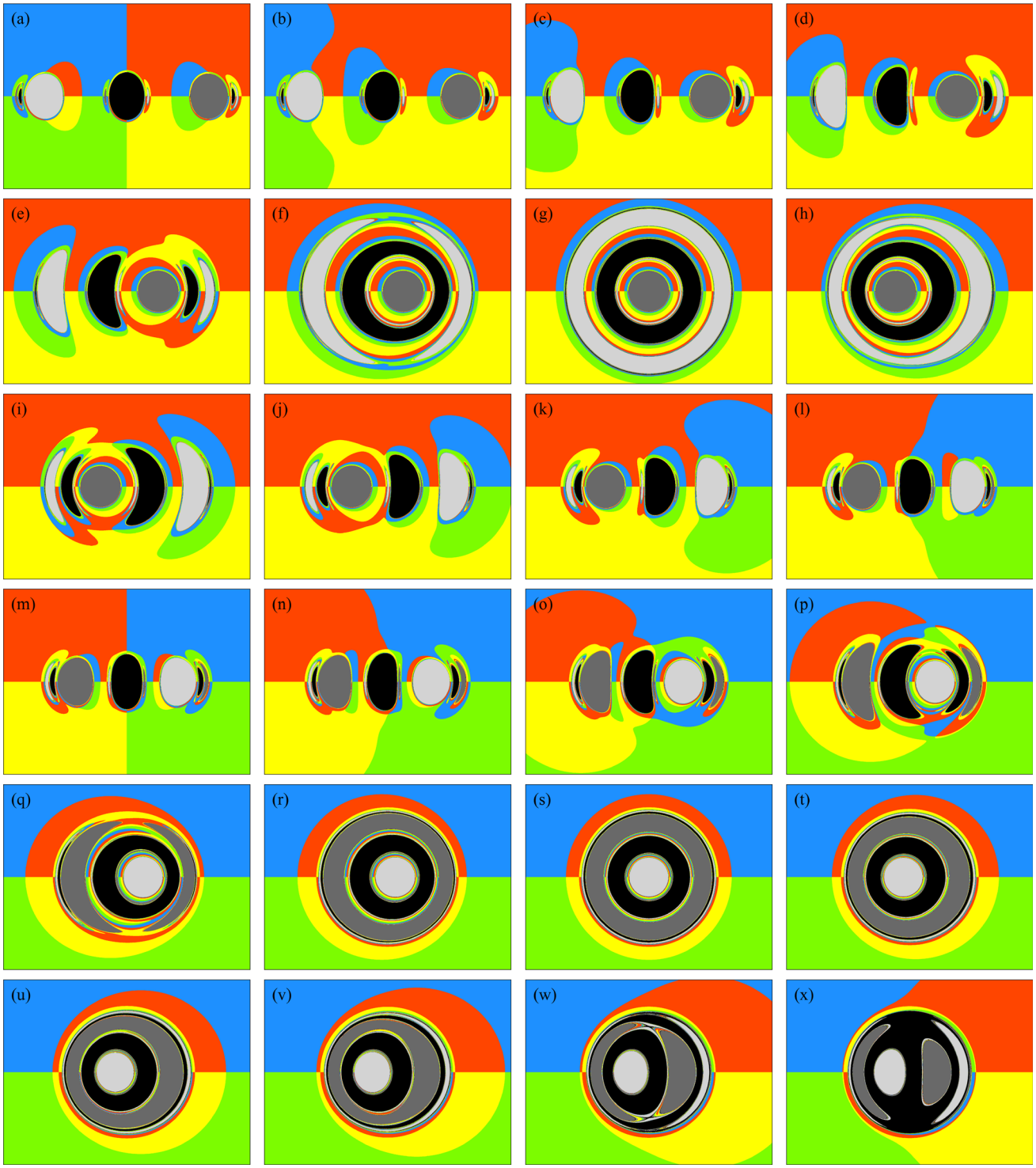

Fig. 6 Shadows of triple black holes across varying separations l and azimuthal angles Φ. From panel **a** to **x**, the separation decreases from $l = 4$ to 0.1 in increments of $\delta l \approx -0.1695$, while Φ ranges from 0° to 345° with $\delta\Phi = 15°$ intervals, all at a fixed observation inclination of $\Theta = 90°$. These results provide qualitative insights into shadow evolution during the inspiral and merger phases of triple black hole systems

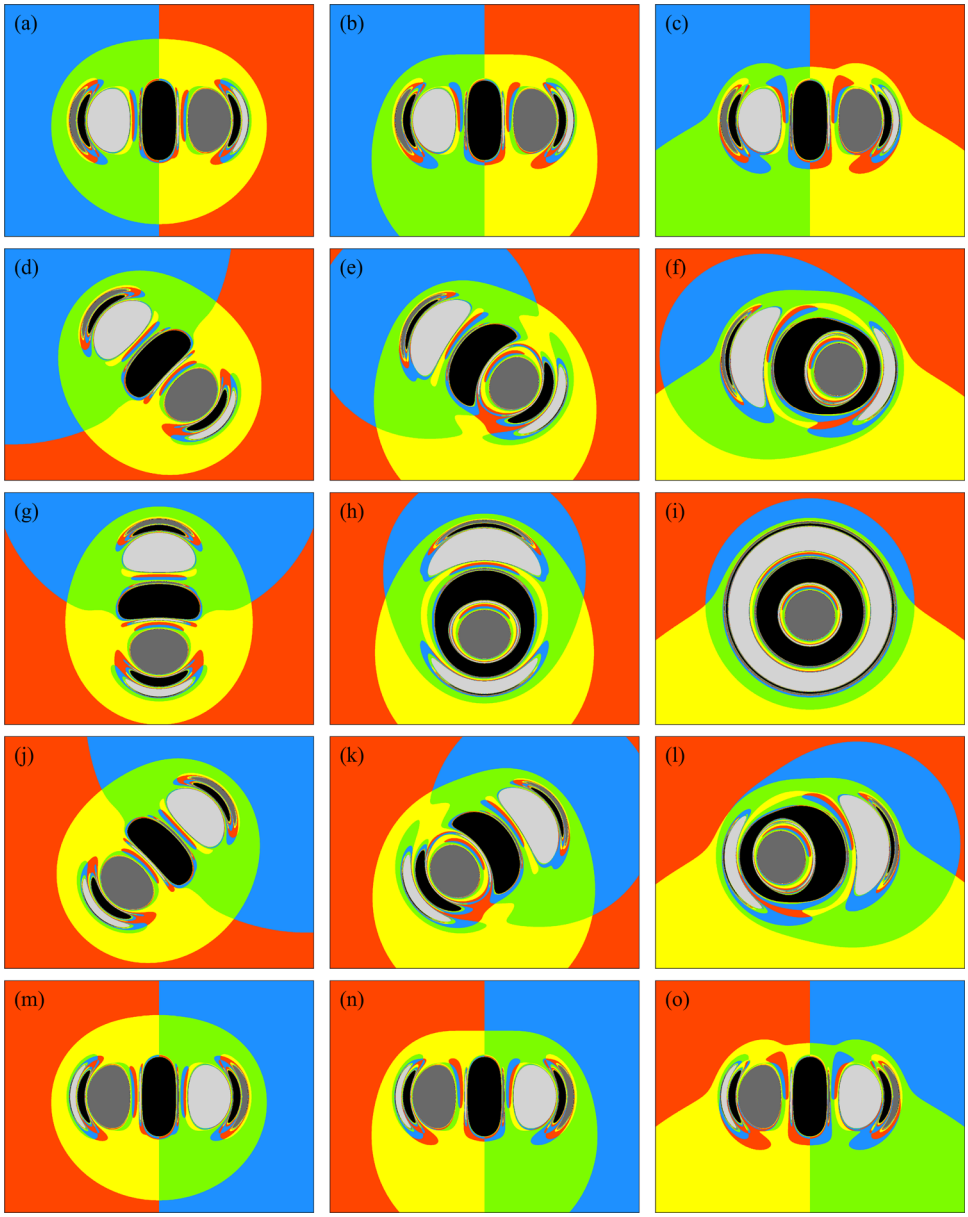

Fig. 7 Shadow morphology of triple black holes at fixed separation $l = 1.2$ for varying observation inclinations Θ and azimuthal angles Φ. From left to right: $\Theta = 17°$, $\Theta = 50°$, and $\Theta = 80°$. From top to bottom: $\Phi = 0°$, $\Phi = 45°$, $\Phi = 90°$, $\Phi = 135°$, and $\Phi = 180°$. The shadow contours exhibit Θ-independent features in the cases of $\Phi = 0°$ and $\Phi = 180°$, whereas under other configurations, the inclination angle significantly rotate the black hole shadows and modulate the strength of gravitational lensing effects

the inclination angle induces significant rotation and deformation of the black hole shadows. This occurs because in these configurations, the triple black hole system is no longer symmetric about the line of sight, and varying the viewing angle consequently modifies the gravitational lensing effects.

4.2 Triangular configuration

In the following numerical simulation, we set the observation plane with $x' \in [-8, 8]\ M_s$ and $y' \in [-8, 8]\ M_s$ at a resolution of 2000×2000 pixels. Figure 8 demonstrates the influence of both the inclination angle Θ and side length l on the shadows when the three black holes are positioned at the vertices of an equilateral triangle. When l is small (first row), we observe that the shadows of the three black holes are closely interconnected, with their positions and shapes strongly dependent on the inclination angle. Notably, despite the extreme proximity of the black holes, their shadows do not merge into a seamless structure as seen in the colinear case. Instead, distinct small-scale bright spots become clearly visible. As l increases, we observe a growth in the size of the bright spots. Simultaneously, the shadows of the three black holes progressively migrate toward the field boundary while undergoing significant morphological changes. Eyebrow-like secondary shadows emerge with larger l, though their spatial distribution depends critically on the inclination angle Θ. For instance, at $\Theta = 45°$ or $\Theta = 90°$, the secondary shadows of m_1 and m_3 flank the quasi-circular shadow of m_2, as exemplified in panels (e), (f), (h), and (i). Notably, these features are entirely absent in the $\Theta = 0°$ case. As the black holes separate further, their shadows progressively separate. Remarkably, regardless of the observer's inclina-

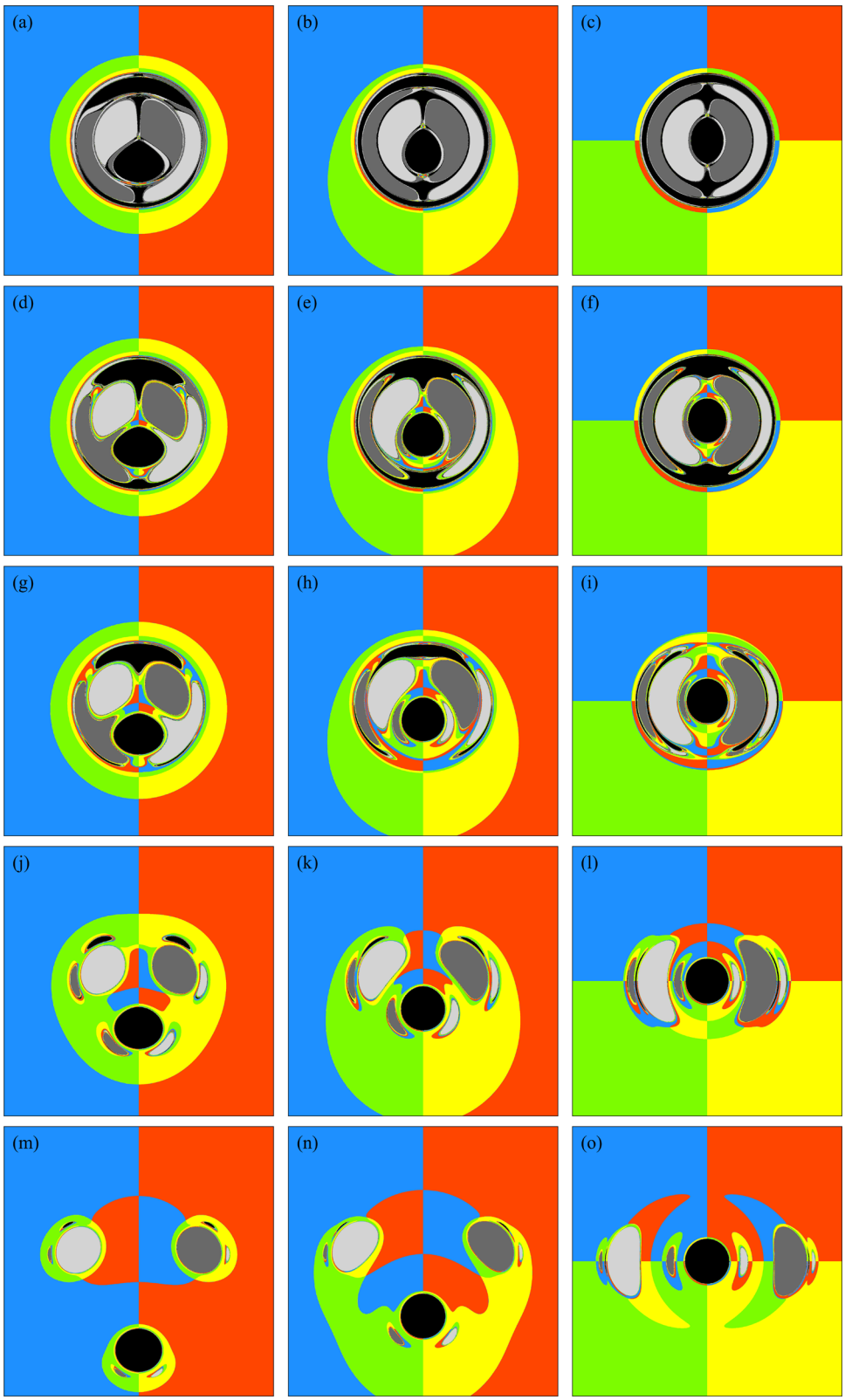

Fig. 8 Three black hole shadows with different parameters in the case of equilateral triangle configuration. From left to right, the observation angles are 0°, 45°, and 90°; from top to bottom, the separation l take values of 0.02, 0.5, 1, 2, and 5. Here, we have the observation azimuth of $\Phi = 0°$

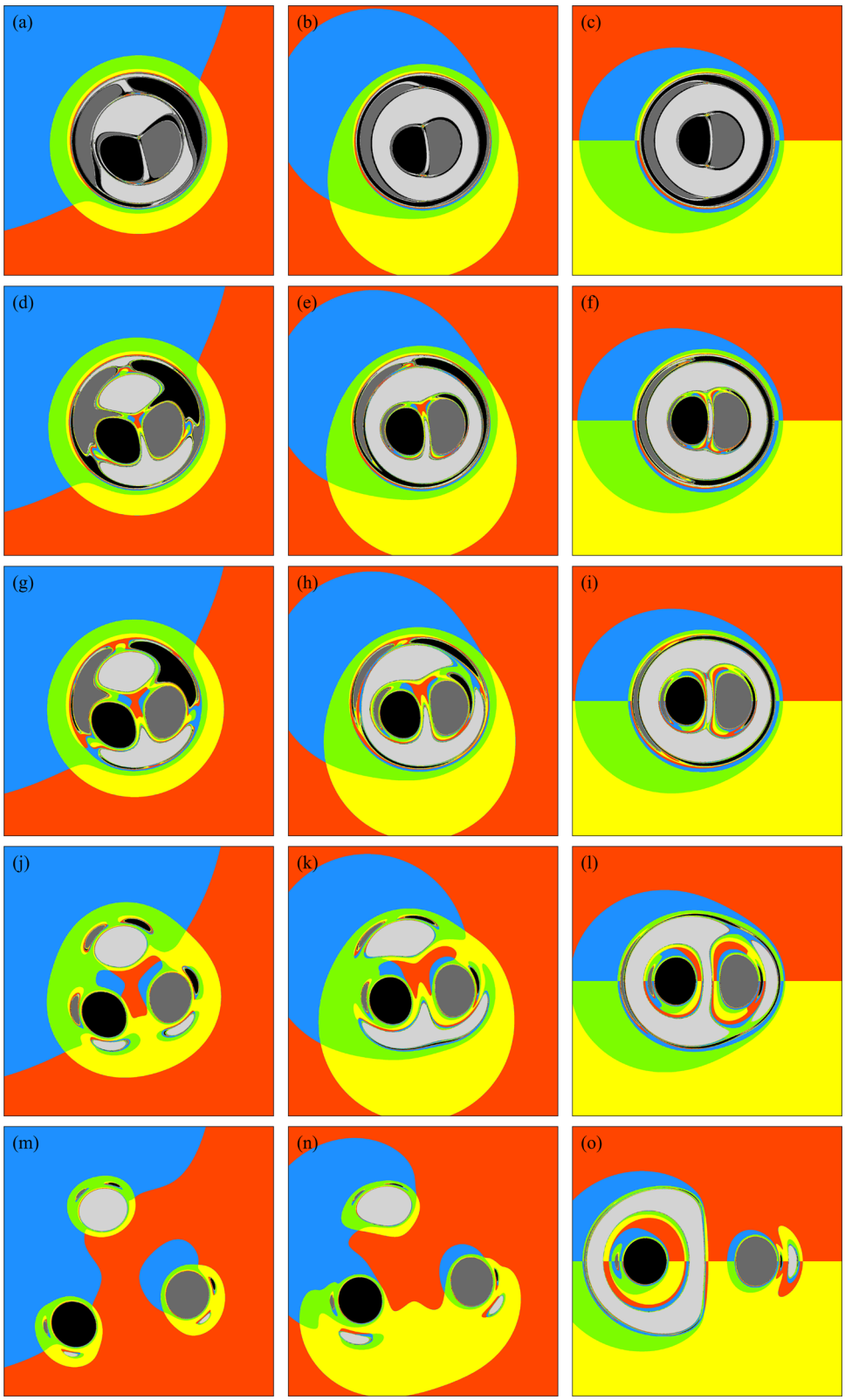

Fig. 9 Similar to Fig. 8, but for an azimuthal angle of $\Phi = 45°$

tion angle, each black hole consistently exhibits at least two clearly identifiable eyebrow-shaped secondary shadows.

We changed the observation azimuth to 45° and repeated the numerical simulations as shown in Fig. 8, with the results presented in Fig. 9. It is evident that as l increases, the trends in the changes of the three black hole shadows are similar to those in Fig. 8, i.e., the shadows deform while also moving toward the screen boundary, accompanied by the formation of multiple eyebrow-like shadows. The deformation and movement directions of the shadows are related to the observation angle. Furthermore, we observed some unique features: First, when the observation inclination is 0° or 45°, the symmetry of the image about the y'-axis is broken. Specifically, m_3 exhibits irregular shadows, as shown in panels (h) and (k). Second, we identified shadow rings caused by gravitational lensing, as seen in panels (l) and (o). This is due to m_3 appearing behind m_2.

5 Conclusions and discussions

By utilizing the Majumdar–Papapetrou solution, we numerically simulated the shadows of three black holes in static equilibrium. We found that the contours of the three black holes' shadow are influenced by the black hole separation, spatial arrangement, and observational parameters. When the three black holes are collinear, each black hole exhibits not only a large, nearly circular primary shadow but also at least two secondary shadows with eyebrow-like features. It is noteworthy that eyebrow-like secondary shadows are not unique to triple black hole systems. Such features have also been identified in simulations of binary black holes [42–45,47,48], scalar hairy black holes [61–63], and distorted single black holes [64,65]. However, the number of eyebrow-like secondary shadows observed in these models is fewer than those reported in our current work. As the black hole separation decreases, both the size and shape of the primary shadows undergo substantial alterations, accompanied by elongation of the secondary shadows. This observation suggests that the shadow morphology can be used to probe three black holes and infer their separation. When the line of sight aligns with the three black holes, shadow rings induced by gravitational lensing are observable, with their size being dependent on the black hole separation. In configurations where the black holes form the vertices of an equilateral triangle, the shadow structure can still exhibit collinear-like features, such as eyebrow-like shadows and ring-shaped shadows. However, substantial differences remain between these images and those arising from collinear configurations. Hence, it is feasible to infer the geometric configuration of a triple black hole system from the observed shadows. Furthermore, regardless of the spatial distribution of the three black holes, we observed self-similar fractal structures at the boundaries of both the primary and secondary shadows, which arise from chaotic scattering of the photon due to the non-integrability of spacetime.

Additionally, we found that when the black hole separation becomes sufficiently small, the shadows of three black holes merge into a standard disk, which can be cast by a single massive, spherically symmetric black hole. This suggests a degeneracy in the light-capturing ability between three sufficiently close extremal RN black holes and a single black hole. This raises the intriguing possibility that an astrophysical black hole observed in the universe might, in fact, be the collective manifestation of multiple closely packed extremal RN black holes.

This study focused primarily on the influence of black hole separation, configuration, and observational parameters on the shadow structure, which not only reveals the connection between parameters and shadows, but also reflects the potential shadow evolution of the three black holes during the process of merging and inspiral. In addition, the Majumdar–Papapetrou solution also incorporates mass parameters, which warrants further exploration of the shadow characteristics of three black holes with varying masses. This will be addressed in future work.

Acknowledgements The authors are very grateful to the referee for insightful comments and valuable suggestions. This research has been supported by the National Natural Science Foundation of China [Grant No. 12403081].

Funding This work was supported by the National Natural Science Foundation of China (Grant No. 12403081).

Data Availability Statement This manuscript has no associated data. [Author's comment: Data sharing not applicable to this article as no datasets were generated or analysed during the current study.]

Code Availability Statement Code/software will be made available on reasonable request. [Author's comment: The code/software generated during and/or analysed during the current study is available from the corresponding author on reasonable request.]

Funded by SCOAP[3].

References

1. K. Akiyama et al. (Event Horizon Telescope Collaboration), First M87 event horizon telescope results. I. The shadow of the supermassive black hole. Astrophys. J. Lett. **875**, L1 (2019)
2. K. Akiyama et al. (Event Horizon Telescope Collaboration), First Sagittarius A* event horizon telescope results. I. The Shadow of the supermassive black hole in the center of the milky way. Astrophys. J. Lett. **930**, L12 (2022)
3. S.E. Gralla, D.E. Holz, R.M. Wald, Black hole shadows, photon rings, and lensing rings. Phys. Rev. D **100**, 024018 (2019)
4. A. Chael, M.D. Johnson, A. Lupsasca, Observing the inner shadow of a black hole: a direct view of the event horizon. Astrophys. J. **918**, 6 (2021)
5. G.P. Li, K.J. He, Shadows and rings of the Kehagias–Sfetsos black hole surrounded by thin disk accretion. J. Cosmol. Astropart. Phys. **06**, 037 (2021)
6. J. Peng, M.Y. Guo, X.H. Feng, Influence of quantum correction on black hole shadows, photon rings, and lensing rings. Chin. Phys. C **45**, 085103 (2021)
7. S.Y. Hu, C. Deng, D. Li, X. Wu, E.W. Liang, Observational signatures of Schwarzschild-MOG black holes in scalar–tensor–vector gravity: shadows and rings with different accretions. Eur. Phys. J. C **82**, 885 (2022)
8. X.X. Zeng, K.J. He, G.P. Li, Effects of dark matter on shadows and rings of Brane-World black holes illuminated by various accretions. Sci. China Phys. Mech. Astron. **65**, 290411 (2022)
9. Y.H. Hou, Z.Y. Zhang, H.P. Yan, M.Y. Guo, B. Chen, Image of a Kerr–Melvin black hole with a thin accretion disk. Phys. Rev. D **106**, 064058 (2022)
10. M. Heydari-Fard, M. Heydari-Fard, N. Riazi, Shadows and photon rings of a spherically accreting Kehagias–Sfetsos black hole. Int. J. Mod. Phys. D **32**, 2350088 (2023)
11. S.Y. Hu, C. Deng, S. Guo, X. Wu, E.W. Liang, Observational signatures of Schwarzschild-MOG black holes in scalar–tensor–vector gravity: images of the accretion disk. Eur. Phys. J. C **83**, 264 (2023)
12. Y. Meng, X.M. Kuang, X.J. Wang, B. Wang, J.P. Wu, Images from disk and spherical accretions of hairy Schwarzschild black holes. Phys. Rev. D **108**, 064013 (2023)
13. J.S. Yang, C. Zhang, Y.G. Ma, Shadow and stability of quantum-corrected black holes. Eur. Phys. J. C **83**, 619 (2023)
14. X.J. Gao, T.T. Sui, X.X. Zeng, Y.S. An, Y.P. Hu, Investigating shadow images and rings of the charged Horndeski black hole illuminated by various thin accretions. Eur. Phys. J. C **83**, 1052 (2023)
15. S.Y. Hu, D. Li, C. Deng, X. Wu, E.W. Liang, Influences of tilted thin accretion disks on the observational appearance of hairy black holes in Horndeski gravity. J. Cosmol. Astropart. Phys. **04**, 089 (2024)
16. T.T. Sui, Z.L. Wang, W.D. Guo, The effect of scalar hair on the charged black hole with the images from accretions disk. Eur. Phys. J. C **84**, 441 (2024)
17. K.J. He, G.P. Li, C.Y. Yang, X.X. Zeng, Optical appearance of a boson star with soliton potential. arXiv:2502.16623
18. K.J. He, H. Ye, X.X. Zeng, L.F. Li, P. Xu, The shadow and accretion disk images of the rotation loop quantum black bounce. arXiv:2502.08388
19. X.X. Zeng, C.Y. Yang, Y.X. Huang, K.J. He, G.P. Li, S. Guo, Optical images of mini boson stars in Palatini f(R) gravity. arXiv:2501.13764
20. K.J. He, C.Y. Yang, X.X. Zeng, Optical appearance of the Konoplya–Zhidenko rotating non-Kerr black hole surrounded by a thin accretion disk. arXiv:2501.06778
21. S.Y. Hu, D. Li, C. Deng, Novel inner shadows of the Kerr black hole with a tilted thin accretion disk. J. Cosmol. Astropart. Phys. **06**, 036 (2025)
22. Y.H. Hou, J.W. Huang, M.Y. Guo, Y. Mizuno, B. Chen, Near-horizon polarization as a diagnostic of black hole spacetime. Astrophys. J. Lett. **988**, L51 (2025)
23. X. Lu, Y. Xie, Gravitational lensing by a quantum deformed Schwarzschild black hole. Eur. Phys. J. C **81**, 627 (2021)
24. Y.X. Gao, Y. Xie, Gravitational lensing by hairy black holes in Einstein-scalar–Gauss–Bonnet theories. Phys. Rev. D **103**, 043008 (2021)
25. X.M. Kuang, Z.Y. Tang, B. Wang, A.Z. Wang, Constraining a modified gravity theory in strong gravitational lensing and black hole shadow observations. Phys. Rev. D **106**, 064012 (2022)
26. Q. Qi, Y. Meng, X.J. Wang, X.M. Kuang, Gravitational lensing effects of black hole with conformally coupled scalar hair. Eur. Phys. J. C **83**, 1043 (2023)
27. G.S. He, Y. Xie, C.H. Jiang, W.B. Lin, Gravitational lensing of massive particles by a black-bounce-Schwarzschild black hole. Phys. Rev. D **110**, 064008 (2024)
28. M.I. Aslam, X.X. Zeng, R. Saleem, X.Y. Hu, Holographic Einstein ring of a charged Rastall AdS black hole with bulk electromagnetic field. Chin. Phys. C **48**, 115101 (2024)
29. X.Y. Hu, M.I. Aslam, R. Saleem, X.X. Zeng, Dynamics of holographic images of scalar–tensor–vector gravity-AdS black holes. Chin. Phys. C **48**, 095108 (2024)
30. X.X. Zeng, L.F. Li, P. Li, B. Liang, P. Xu, Holographic images of a charged black hole in Lorentz symmetry breaking massive gravity. Sci. China Phys. Mech. Astron. **68**, 220412 (2025)
31. M. Heydari-Fard, H.R. Sepangi, Thin accretion disk signatures of scalarized black holes in Einstein-scalar–Gauss–Bonnet gravity. Phys. Lett. B **816**, 136276 (2021)
32. C. Liu, T. Zhu, Q. Wu, Thin accretion disk around a four-dimensional Einstein Gauss–Bonnet black hole. Chin. Phys. C **45**, 015105 (2021)
33. K. Boshkayev, T. Konysbayev, Y. Kurmanov, O. Luongo, D. Malafarina, Accretion disk luminosity for black holes surrounded by dark matter with tangential pressure. Astrophys. J. **936**, 96 (2022)
34. M. Heydari-Fard, S.G. Honarvar, M. Heydari-Fard, Thin accretion disc luminosity and its image around rotating black holes in perfect fluid dark matter. Mon. Not. R. Astron. Soc. **521**, 708 (2023)
35. K. Boshkayev, T. Konysbayev, Y. Kurmanov, O. Luongo, M. Muccino, A. Taukenova, A. Urazalina, Luminosity of accretion disks around rotating regular black holes. Eur. Phys. J. C **84**, 230 (2024)
36. M.D. Johnson et al., Key science goals for the next-generation event horizon telescope. Galaxies **11**, 61 (2023)
37. P. Galison et al., The next generation event horizon telescope collaboration history, philosophy, and culture. Galaxies **11**, 32 (2023)
38. K.M. Shavelle, D.C.M. Palumbo, Prospects for the detection of the Sgr A* photon ring with next-generation event horizon telescope polarimetry. Astrophys. J. Lett. **970**, L24 (2024)
39. H. Sudou, S. Iguchi, Y. Murata, Y. Taniguchi, Orbital motion in the radio galaxy 3C 66B: evidence for a supermassive black hole binary. Science **300**, 1263 (2003)
40. A. Sillanpää, S. Haarala, M.J. Valtonen, B. Sundelius, G.G. Byrd, OJ 287: binary pair of supermassive black holes. Astrophys. J. **325**, 628 (1988)
41. E. Vitral, G.A. Mamon, Does NGC 6397 contain an intermediate-mass black hole or a more diffuse inner subcluster? Astron. Astrophys. **646**, A63 (2021)
42. D. Nitta, T. Chiba, N. Sugiyama, Shadows of colliding black holes. Phys. Rev. D **84**, 063008 (2011)
43. A. Yumoto, D. Nitta, T. Chiba, N. Sugiyama, Shadows of multi-black holes: analytic exploration. Phys. Rev. D **86**, 103001 (2012)
44. A. Bohn, W. Throwe, F. Hébert, K. Henriksson, D. Bunandar, M.A. Scheel, N.W. Taylor, What does a binary black hole merger look like? Class. Quantum Gravity **32**, 065002 (2015)
45. P.V.P. Cunha, C.A.R. Herdeiro, M.J. Rodriguez, Shadows of exact binary black holes. Phys. Rev. D **98**, 044053 (2018)

46. S.V. Chernov, Shadows and photon rings of binary black holes. Gravit. Cosmol. (Russia) **30**, 165 (2024)
47. J.O. Shipley, S.R. Dolan, Binary black hole shadows, chaotic scattering and the Cantor set. Class. Quantum Gravity **33**, 175001 (2016)
48. Z.S. Moreira, C.A.R. Herdeiro, L.C.B. Crispino, Spinning generalizations of Majumdar–Papapetrou multi-black hole spacetimes: light rings, lensing and shadows. arXiv:2502.01759
49. S. Majumdar, A class of exact solutions of Einstein's field equations. Phys. Rev. **72**, 390 (1947)
50. A. Papaetrou, A static solution of the equations of the gravitational field for an arbitrary charge distribution. Proc. R. Ir. Acad. A **51**, 191 (1947)
51. J.B. Hartle, S.W. Hawking, Solutions of the Einstein–Maxwell equations with many black holes. Commun. Math. Phys. **26**, 87 (1972)
52. Y. Wang, G.Q. Shen, X. Sun, The space-time properties of three static black holes. Symmetry **15**, 702 (2023)
53. F.H. Vincent, T. Paumard, E. Gourgoulhon, G. Perrin, GYOTO: a new general relativistic ray-tracing code. Class. Quantum Gravity **28**, 225011 (2011)
54. C. Bambi, A code to compute the emission of thin accretion disks in non-Kerr space-times and test the nature of black hole candidates. Astrophys. J. **761**, 174 (2012)
55. P.V.P. Cunha, C.A.R. Herdeiro, E. Radu, H.F. Rúnarsson, Shadows of Kerr black holes with and without scalar hair. Int. J. Mod. Phys. D **25**, 1641021 (2016)
56. Z.Z. Hu, Z. Zhong, P.C. Li, M.Y. Guo, B. Chen, QED effect on a black hole shadow. Phys. Rev. D **103**, 044057 (2021)
57. J.M. Velsquez-Cadavid, J.A. Arrieta-Villamizar, F.D. Lora-Clavijo, O.M. Pimentel, J.E. Osorio-Vargas, OSIRIS: a new code for ray tracing around compact objects. Eur. Phys. J. C **82**, 103 (2022)
58. J.W. Huang, L.H. Zheng, M.Y. Guo, B. Chen, Coport: a new public code for polarized radiative transfer in a covariant framework. J. Cosmol. Astropart. P. **11**, 054 (2024)
59. H.Y. Pu, K. Yun, Z. Younsi, S.J. Yoon, Odyssey: a public GPU-based code for general-relativistic radiative transfer in Kerr spacetime. Astrophys. J. **820**, 105 (2016)
60. Z. Younsi, A. Zhidenko, L. Rezzolla, R. Konoplya, Y. Mizuno, New method for shadow calculations: application to parametrized axisymmetric black holes. Phys. Rev. D **94**, 084025 (2016)
61. P.V.P. Cunha, C.A.R. Herdeiro, E. Radu, H.F. Rúnarsson, Shadows of Kerr black holes with scalar hair. Phys. Rev. Lett. **115**, 211102 (2015)
62. P.V.P. Cunha, J. Grover, C. Herdeiro, E. Radu, H. Rúnarsson, A. Wittig, Chaotic lensing around boson stars and Kerr black holes with scalar hair. Phys. Rev. D **94**, 104023 (2016)
63. G.N. Gyulchev, A. Roy, L.G. Collodel, P.G. Nedkova, S.S. Yazadjiev, D.D. Doneva, Shadows of rotating hairy Kerr black holes coupled to time periodic scalar fields with non-flat target space. Phys. Rev. D **109**, 104051 (2024)
64. S. Abdolrahimi, R.B. Mann, C. Tzounis, Double images from a single black hole. Phys. Rev. D **92**, 124011 (2015)
65. J. Grover, J. Kunz, P. Nedkova, A. Wittig, S. Yazadjiev, Multiple shadows from distorted static black holes. Phys. Rev. D **97**, 084024 (2018)